ACS Energy LETTERS

http://pubs.acs.org/journal/aelccp

Letter

Heptacyclic Ladder-Type Triarylamine-Functionalized Polymers as Hole-Transporting Layers with Stirring-Controlled Aggregation for Efficient and Stable Tin Perovskite Solar Cells

Chia-Fang Lu,[⊥] Yun-Sheng Shih,[⊥] Chun-Hsiao Kuan, Yu-An Ko, Hsin-Lung Chen, Yen-Ju Cheng,* and Eric Wei-Guang Diau*

Cite This: https://doi.org/10.1021/acsenergylett.6c00952

Read Online

ACCESS | Metrics & More | Article Recommendations | Supporting Information

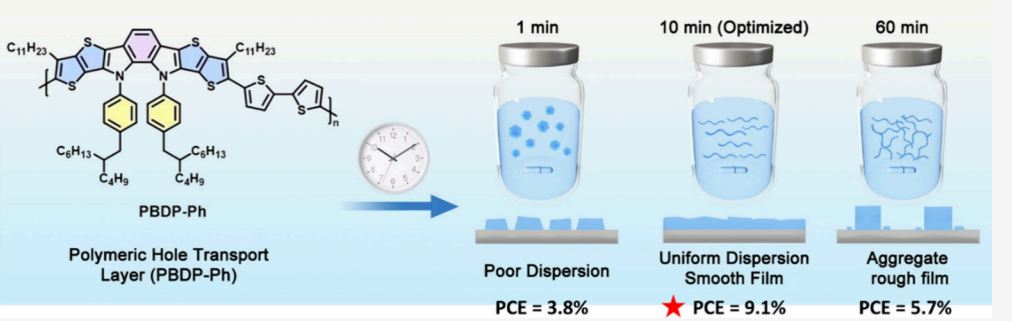

ABSTRACT: Tin-based perovskite solar cells (TPSCs) are promising lead-free photovoltaics but remain limited by inefficient hole extraction, interfacial recombination, and poor operational stability. Here, we report a series of benzodipyrrole (BDP)-based conjugated polymer hole-transporting layers (HTLs) with controlled aggregation for inverted TPSCs. By integrating triarylamine-like aryl substitution into a rigid, coplanar BDP ladder backbone, a polymeric PBDP-Ph HTL with favorable energy-level alignment, high hole mobility, and improved interfacial compatibility was synthesized. Beyond molecular design, we identify stirring time of the polymer precursor solution as a critical parameter governing solution-state aggregation, film morphology, and device performance. An optimal stirring duration of 10 min yields well-dispersed polymer chains, smooth HTL films, and high-quality perovskite crystallization, thereby suppressing nonradiative recombination and enhancing charge extraction. Consequently, TPSC employing PBDP-Ph fabricated via a two-step approach delivers a power conversion efficiency of 9.1%, outperforming conventional PEDOT:PSS-based and other BDP-derived devices, while exhibiting markedly improved long-term and operational stability.

Perovskite solar cells (PSCs) have attracted tremendous attention in the photovoltaic community owing to their low fabrication cost and remarkable power conversion efficiencies (PCEs). To date, single-junction lead-containing PSCs have achieved a certified PCE of 27%.[1,2] However, the toxicity of lead raises serious environmental and health concerns, thereby impeding large-scale commercialization. In this context, tin-based perovskite solar cells (TPSCs) have emerged as a promising lead-free alternative, combining reduced toxicity with a higher theoretical efficiency. Recent TPSCs studies have already achieved PCEs exceeding 17%.[3,4] However, tin-based perovskites generally suffer from Sn^{2+} oxidation and poor intrinsic stability. To address these issues, we recently adopted a two-step cosolvent-assisted fabrication method.[5−9] SnF_2 was added to the SnI_2 precursor to suppress Sn^{2+} oxidation, forming a stable Sn^{2+}-rich intermediate. Unlike conventional one-step antisolvent processes that induce rapid crystallization and phase segregation, the two-step approach enables controlled nucleation and crystal growth via a transient SnI_2−DMSO intermediate, allowing gradual conversion to high-quality $FASnI_3$ films upon FAI deposition.

Inverted PSCs offer key advantages, including low-temperature processing, improved stability, negligible hysteresis, and compatibility with flexible and tandem applications.[10−17] Consequently, significant efforts have focused on enhancing inverted PSCs via perovskite composition and bandgap engineering, optimization of charge-transport layers, and surface passivation strategies.[18−29] Among these strategies, optimization of the hole-transporting layer (HTL) is particularly effective, highlighting the importance of rational hole-transporting material (HTM) design. In inverted PSCs,

Received: March 28, 2026
Revised: May 4, 2026
Accepted: May 6, 2026

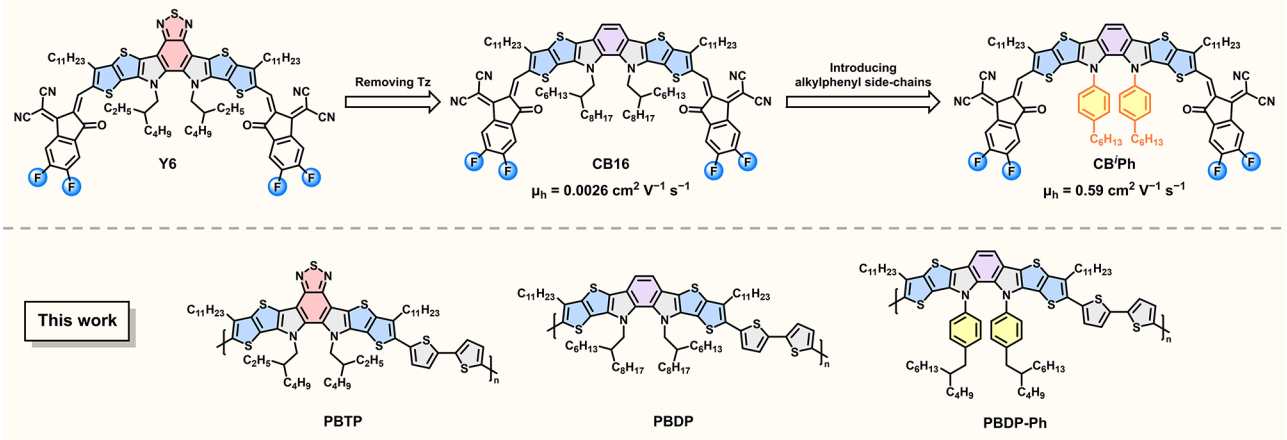

Figure 1. Chemical structures showing Y6, CB16, and CB^{i}Ph nonfullerene acceptors as well as **PBTP**, **PBDP**, and **PBDP-Ph** polymers reported in this work.

Scheme 1. Synthetic Routes of BDP-Ph Monomer and Three PBTP, PBDP, and PBDP-Ph Polymers

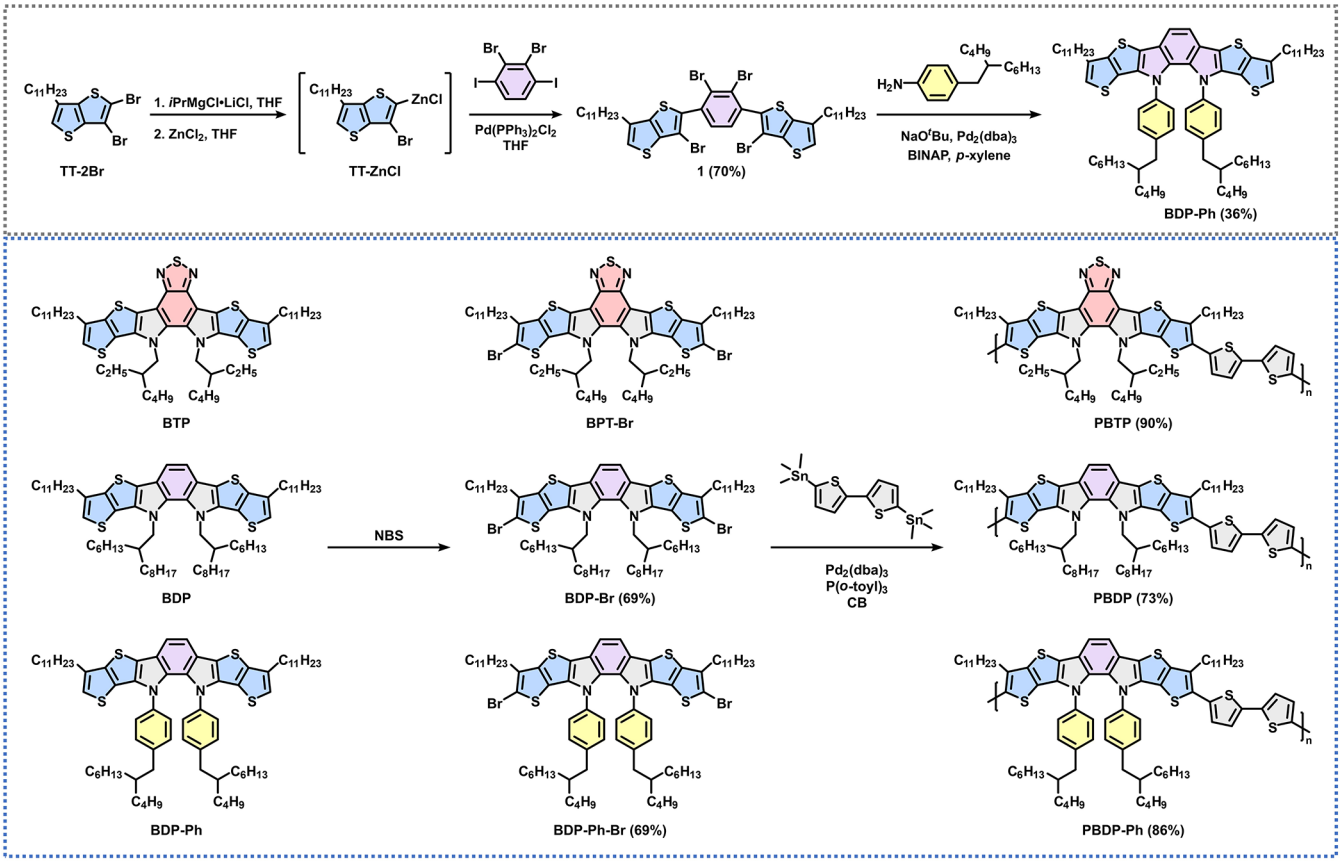

the HTL is responsible for efficient hole extraction and transport, suppression of electron backflow and interfacial recombination, and provision of suitable surface wettability for uniform perovskite crystallization.[30−35] Consequently, HTM molecular design and interfacial compatibility critically govern both device efficiency and operational stability.

HTMs can be broadly classified into metal oxides, organic small molecules, and conjugated polymers. Metal oxides offer low cost, high conductivity, and chemical robustness but often suffer from interfacial defects. Organic small molecules provide precise energy-level tunability yet typically exhibit poor film formation and thermal instability. In contrast, conjugated polymers combine solution processability, tunable energy levels, high charge mobility, and enhanced stability, making them promising HTMs for both Pb- and Sn-based PSCs. Among them, PEDOT:PSS is the most widely used polymeric HTM in inverted PSCs and TPSCs.[36] However, its hydrophilicity and acidity lead to poor perovskite crystallinity, reduced fill factor, and accelerated degradation, underscoring the need for alternative polymeric HTMs with improved interfacial compatibility and stability.[37]

Recent advances in organic semiconductors for organic solar cells (OSCs) have provided useful insights for HTM design.[38,39] Y6 and its derivatives, featuring a heptacyclic

https://doi.org/10.1021/acsenergylett.6c00952
ACS Energy Lett. XXXX, XXX, XXX−XXX

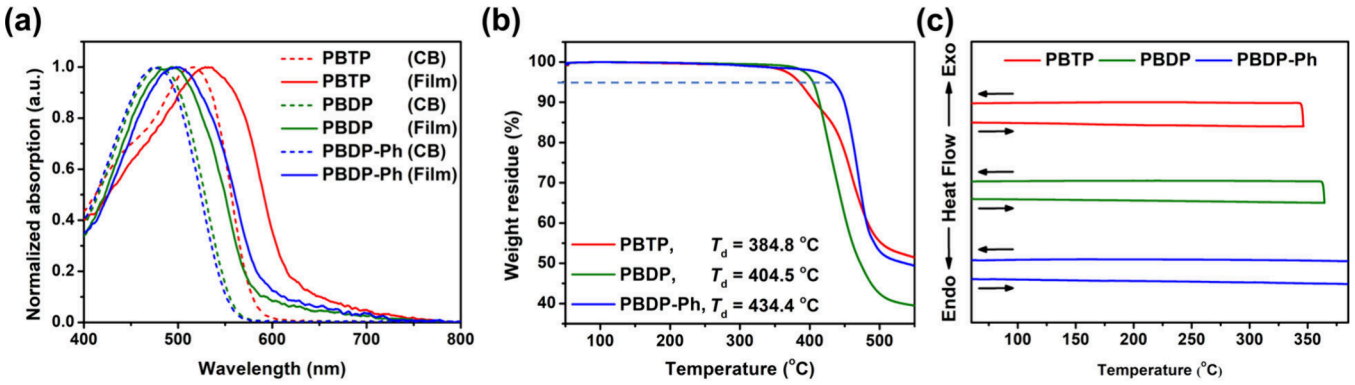

Figure 2. Normalized absorption spectra (a) of **PBTP**, **PBDP**, and **PBDP-Ph** in CB and thin films, (b) TGA and (c) DSC measurements of **PBTP**, **PBDP**, and **PBDP-Ph** with a ramping rate of 10 °C/min.

Table 1. Molecular Weights, Optical Properties, and Decomposition Temperatures of PBTP, PBDP, and PBDP-Ph

	M_n		λ_{max} (nm)		$\Delta\lambda$	λ_{onset}	E_g^{opt}	T_d
Polymers	(kDa)	Đ	CB	Film	(nm)	(nm)[a]	(eV)[b]	(°C)
PBTP	28.3	1.87	517	535	18	624	1.99	384.8
PBDP	37.2	1.78	483	492	9	586	2.12	404.5
PBDP-Ph	39.4	1.74	473	499	26	593	2.09	434.4

[a]Calculated in the solid state. [b]$E_g^{opt} = 1240/\lambda_{onset}$.

fused-ring benzothiadiazoledipyrrole-thieno[3,2-*b*]thiophene (BTP) framework,[40,41] have emerged as highly efficient nonfullerene acceptors (NFAs) in OSCs.[42−45] BTP-based small molecules and polymers have also shown great promise as HTMs in PSCs.[46−50] For example, a BTP-based polymer has been reported as a dopant-free HTL that improves charge transport and passivates perovskite surface defects, leading to a PCE of 22.02%.[47] Along this line, we recently developed a heptacyclic benzodipyrrole-thieno[3,2-*b*]thiophene (BDP) framework that is structurally analogous to BTP but eliminates the central thiadiazole (Tz) unit. The resulting BDP core was subsequently condensed with fluoroindanone (FIC) end groups to afford a new NFA, denoted as CB16.[51] Similar to Y6-type derivatives, CB16 adopts a C-shaped geometry that facilitates three-dimensional grid-like molecular packing, enabling multidirectional charge percolation and efficient charge transport. CB derivatives exhibit not only high electron but also great hole mobilities.[52−59] The electron-rich, rigid and coplanar BDP donor core accounts for the efficient hole transport, suggesting that the BDP framework is well suited for incorporation into conjugated polymers as high-performance HTMs for perovskite solar cells. Triarylamine (TAA) motifs are widely used in HTMs due to their strong hole-extraction capability and high hole mobility, with numerous TAA-based small molecules and polymers demonstrating excellent performance in both PSCs and TPSCs.[60−64] It is envisaged that introducing 4-alkylphenyl substituents at the nitrogen atoms of the BDP core creates a TAA-like architecture with enhanced hole-transporting properties. Accordingly, CB^{i}Ph NFA bearing 4-hexylphenyl substituents on the BDP nitrogen atoms was developed (Figure 1). TAA-substitution effectively reverses the charge-transport polarity from n-type to p-type, yielding hole-dominant transport with a high organic field-effect transistor (OFET) hole mobility of 0.59 $cm^2\ V^{-1}\ s^{-1}$,[53] attributed to enhanced hole-transfer integrals and reduced energetic disorder. This molecular design provides a viable framework for developing BDP-based polymeric HTMs for inverted PSCs.

In this study, we first developed two conjugated alternating copolymers, **PBTP** and **PBDP**, by copolymerizing *N*-alkylated BTP and BDP monomers with a bithiophene monomer through palladium-catalyzed Stille polymerization. To further explore the corresponding TAA-based counterpart, another BDP monomer substituted with 4-(2-butyloctyl)phenyl side chains at nitrogen atoms was designed and synthesized, affording the **PBDP-Ph** polymer. Among the three HTMs, **PBDP-Ph** with 10 min solution stirring time forms the smoothest films, thereby improving interfacial contact and facilitating perovskite crystallization. In addition, **PBDP-Ph** exhibits the lowest-lying energy level, the highest hole mobility, and the most effectively suppressed recombination losses, which are beneficial for efficient hole extraction and transport. Consequently, devices based on **PBDP-Ph** deliver the best photovoltaic performance, achieving a PCE of 9.1%, surpassing those based on **PBTP** (6.3%), **PBDP** (5.3%), and PEDOT:PSS (3.9%). Notably, the 9.1% efficiency represents the highest reported value to date for two-step TPSCs fabricated utilizing a non-PEDOT:PSS HTL. Furthermore, **PBDP-Ph**-based devices exhibit superior long-term and operational stability compared with those based on **PBTP**, **PBDP**, and the widely used PEDOT:PSS.

The synthetic routes for the dibromo monomers **BTP-Br**, **BDP-Br**, and **BDP-Ph-Br** are illustrated in Scheme 1. **BTP** and **BDP** were synthesized following the reported literature procedures.[44,51] Similar to the synthesis of **BDP**, palladium-catalyzed Negishi coupling of the TT-ZnCl reagent with 1,2-dibromo-3,6-diiodobenzene yielded compound **1**, which was then cyclized via Buchwald-Hartwig amination with 4-(2-butyloctyl)phenylamine to afford **BDP-Ph**, featuring 4-alkylphenyl side-chains attached to the BDP nitrogen atoms. Bromination of **BTP**, **BDP** and **BDP-Ph** with *N*-bromosuccinimide (NBS) afforded the corresponding dibromo monomers, **BTP-Br**, **BDP-Br** and **BDP-Ph-Br**, respectively. The

https://doi.org/10.1021/acsenergylett.6c00952
ACS Energy Lett. XXXX, XXX, XXX−XXX

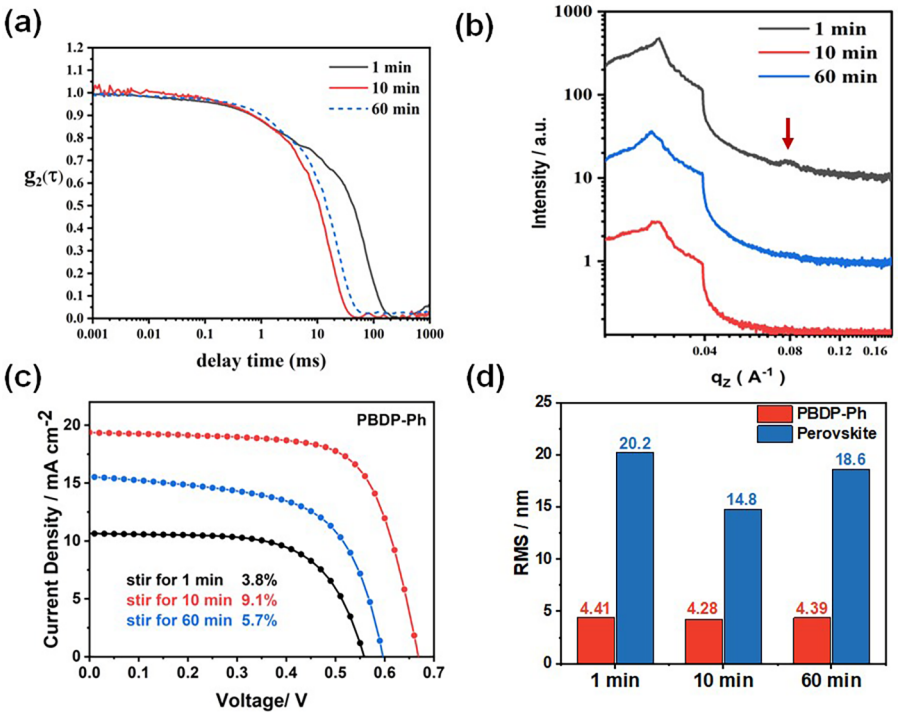

Figure 3. (a) DLS autocorrelation functions $g_2(\tau)$ of **PBDP-Ph** in toluene solutions stirred for 1, 10, and 60 min. (b) GI-SAXS profiles of spin-coated **PBDP-Ph** films processed from the 1-, 10-, and 60 min stirring solutions. (c) *J-V* curves of **PBDP-Ph**-based TPSCs using polymer solutions stirred for different durations. (d) Comparison of AFM root-mean-square (RMS) surface roughness of **PBDP-Ph** polymer films (1, 10, and 60 min), and the corresponding perovskite layers deposited on top of the polymer HTLs.

polymers **PBTP**, **PBDP**, and **PBDP-Ph** were subsequently synthesized through palladium-catalyzed Stille polymerization between the dibromo monomers and 1,1′-[2,2′-bithiophene]-5,5′-diylbis[1,1,1-trimethylstannane]. The number-average molecular weights (M_n) of the resulting polymers were determined by high-temperature gel permeation chromatography (HT-GPC) in trichlorobenzene (the HT-GPC distribution plots are shown in Figure S1). As summarized in Table S1, the M_n values were 28.3, 37.3, and 39.4 kDa for **PBTP**, **PBDP**, and **PBDP-Ph**, respectively. Detailed synthetic procedures and the corresponding ^{1}H, ^{13}C NMR spectra (Figures S2−S12) are provided in Supporting Information.

The absorption spectra of **PBTP**, **PBDP**, and **PBDP-Ph** are presented in Figure 2a, with the corresponding parameters summarized in Table 1. In dilute chlorobenzene (CB) solution, λ_{max} for **PBTP**, **PBDP**, and **PBDP-Ph** are observed at 517, 483, and 473 nm, respectively. The red-shifted absorption of **PBTP** is ascribed to the electron withdrawing benzothiadiazole (BT) unit, which enhances the intramolecular charge transfer (ICT) effect along the polymer backbone. Upon film formation, all three polymers exhibit further red shifts, indicating stronger intermolecular interactions and more compact molecular packing, facilitated by their rigid conjugated backbones. Based on the absorption onsets of the thin films, the optical bandgaps of **PBTP**, **PBDP**, and **PBDP-Ph** are estimated to be 1.99, 2.12, and 2.09 eV, respectively. To evaluate aggregation behavior, the absorption peak shift between solution and film states ($\Delta\lambda$) was analyzed. **PBDP** exhibits the smallest $\Delta\lambda$ (9 nm), followed by **PBTP** (18 nm), while **PBDP-Ph** shows the largest $\Delta\lambda$ (26 nm). The small $\Delta\lambda$ of **PBDP** suggests stronger solution-state aggregation, consistent with its more planar backbone. This is supported by density functional theory (DFT) calculations of molecular geometries at the B3LYP/6−311G (d,p) level (Figure S13), where the BDP unit in **PBDP** displays a smaller torsion angle (7.62°) compared to the BTP unit in **PBTP** (10.83°), thereby promoting intermolecular interaction. In contrast, although BDP-Ph unit in **PBDP-Ph** shows a comparable backbone torsion angle (10.32°) to that of the BTP unit in **PBTP**, the presence of aryl substituents introduces steric hindrance that suppresses excessive aggregation in solution. The thermal properties of the polymers were examined using thermogravimetric analysis (TGA) measurements and differential scanning calorimetry (DSC), as shown in Figures 2b and 2c. The decomposition temperatures (T_d) corresponding to 5% weight loss were determined to be 384.8 °C for **PBTP**, 404.5 °C for **PBDP**, and 434.4 °C for **PBDP-Ph**. DSC measurements revealed no noticeable phase transition temperatures for all three polymers, suggesting their amorphous nature.[40]

To examine how the solution-state aggregation of **PBDP-Ph** affects the morphology of the subsequently cast HTL films, polymer/toluene solutions (0.1 mg mL^{-1}) were stirred for 1, 10, and 60 min prior to film spin-coating deposition. The aggregation states were probed by dynamic light scattering (DLS), and the corresponding autocorrelation functions, $g_2(\tau)$, are shown in Figure 3a. A clear dependence on stirring duration is observed. The solution stirred for only 1 min exhibits the slowest decay in $g_2(\tau)$, indicating the presence of large, slowly relaxing aggregates. This behavior is consistent with incomplete dispersion, where the initial polymer powder remains as coarse agglomerates that have not yet been effectively broken apart by shear. Increasing the stirring time to 10 min leads to a pronounced acceleration of the $g_2(\tau)$ decay, signifying a substantial reduction in aggregate size. This indicates that moderate stirring provides sufficient mechanical energy to disrupt powder-derived clusters and produces a

https://doi.org/10.1021/acsenergylett.6c00952
ACS Energy Lett. XXXX, XXX, XXX−XXX

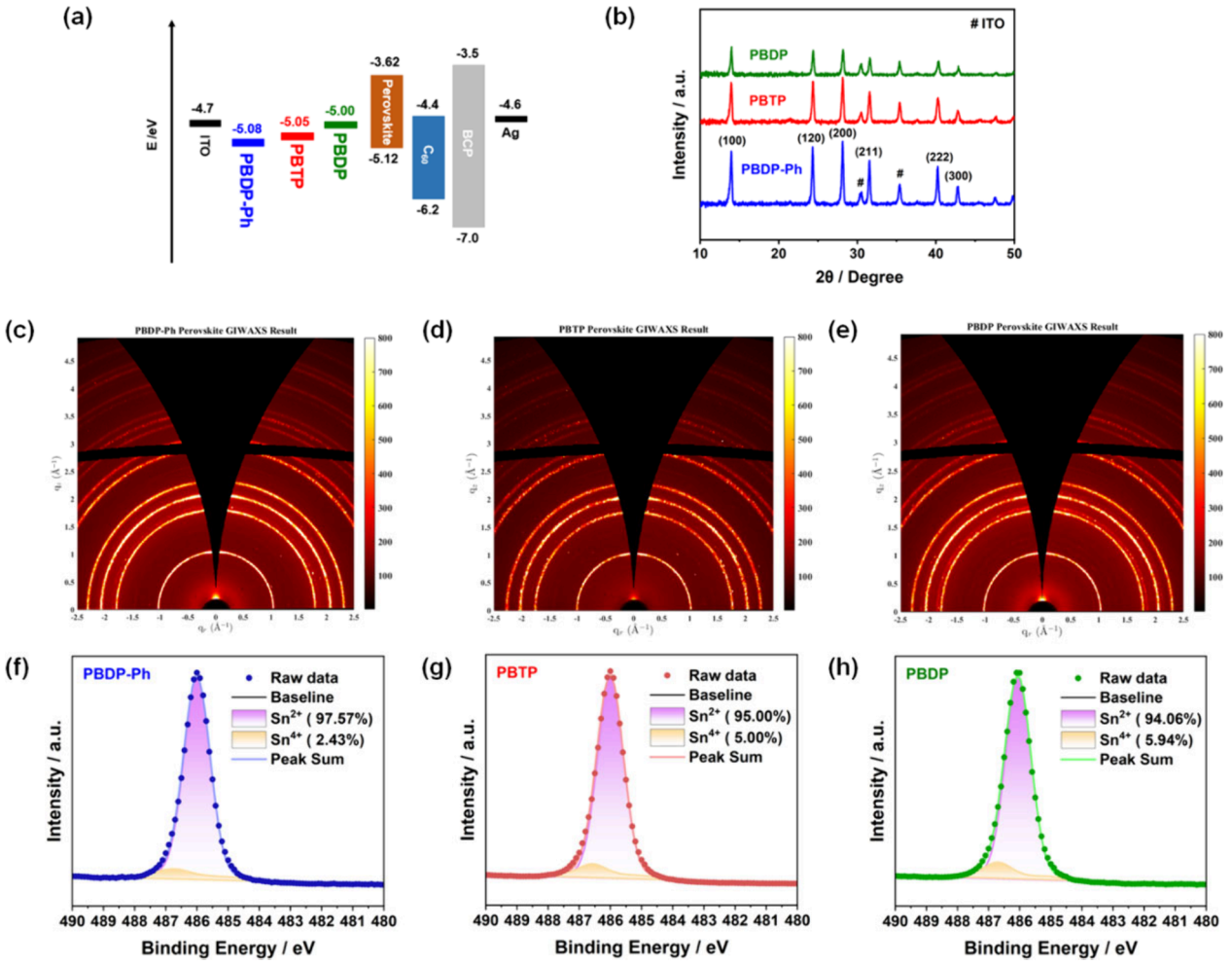

Figure 4. (a) Energy-level diagram of Sn-based perovskite solar cells with the structure ITO/HTL/Sn-based perovskites/C_{60}/BCP/Ag, where **PBDP-Ph**, **PBTP**, and **PBDP** are used as HTLs. (b) XRD patterns of tin perovskite films deposited on **PBDP-Ph**, **PBTP**, and **PBDP** HTLs. (c–e) 2D GIWAXS patterns of Sn-based perovskite films fabricated on **PBDP-Ph**, **PBTP**, and **PBDP** as HTLs, respectively. (f–h) XPS spectra of the Sn 3d core level for tin-based perovskite films deposited on **PBDP-Ph**, **PBTP**, and **PBDP** HTLs, respectively.

relatively homogeneous dispersion of polymer chains or small, weakly associated aggregates.

Interestingly, further extending the stirring time to 60 min reverses this trend, as reflected by a shift of $g_2(\tau)$ toward longer delay times. This clearly indicates the re-emergence of larger or more slowly relaxing structures. Such time-dependent reaggregation under continuous stirring can be rationalized by considering the interplay between shear-induced dispersion and thermodynamically driven association. Specifically, the initial stage of stirring is dominated by mechanical breakup of kinetically trapped powder aggregates. Once these large clusters are disintegrated (≈10 min), the system enters a regime where polymer chains are more uniformly solvated. However, **PBDP-Ph** is a conjugated polymer with strong intermolecular interactions (e.g., $\pi-\pi$ stacking), and its fully dissolved state in a marginal solvent such as toluene is not thermodynamically stable. Under prolonged stirring, the following two key processes can promote reaggregation: (1) Enhanced chain encounters under continuous convection: Sustained stirring increases the frequency of intermolecular collisions. Once the system is fully dispersed, these collisions facilitate interchain association rather than breakup, particularly when attractive interactions are present. (2) Time-dependent conformational relaxation toward lower-energy aggregated states: Initially dispersed chains may adopt relatively extended or nonequilibrium conformations. With time, they relax toward conformations that favor intermolecular stacking and aggregation, leading to the formation of mesoscopic clusters. This process is analogous to solution aging commonly reported in conjugated polymer systems, where aggregation is governed by slow structural reorganization toward thermodynamic equilibrium.[65−67]

Therefore, the 10 min condition represents a transient, nonequilibrium state in which mechanical dispersion dominates over association, while the 60 min condition reflects a re-equilibrated state where thermodynamically driven aggregation becomes significant. This mechanistic picture explains why reaggregation occurs even under continuous stirring: once large clusters are eliminated, further stirring no longer reduces aggregate size but instead accelerates the approach toward an energetically favorable aggregated state.

The distinct dispersion states of these solutions directly influence the nanostructure of the resulting spin-cast films, as revealed by the grazing-incidence small-angle scattering (GI-SAXS) profiles shown in Figure 3b and the GI-SAXS 2D maps in Figure S14. All films exhibit a primary scattering peak near $q_z \approx 0.03$ Å^{-1}, corresponding to a characteristic domain spacing of about 21 nm. However, the sharpness and intensity

https://doi.org/10.1021/acsenergylett.6c00952
ACS Energy Lett. XXXX, XXX, XXX−XXX

of this peak, as well as the presence of higher-order reflections, depend strongly on the prior stirring history of the solution. The film prepared from the 1 min-stirred solution displays the most pronounced structural order: the primary peak is distinctly sharper, and a third-order peak at $q_z \approx 0.09$ Å^{-1} (marked by the arrow) is clearly visible. The 1:3 q-ratio between these peaks implies a lamellar-type periodicity, suggesting the formation of relatively large and well-ordered lamellar domains. In contrast, the films obtained from the 10- and 60 min-stirred solutions exhibit broader and less intense primary peaks, implying reduced domain order or more limited spatial coherence. Notably, among them, the film derived from the 10 min solution shows the weakest overall scattering intensity, indicating the smallest fraction of ordered phase. These results establish a direct and intuitive correlation between solution-state aggregation, stirring duration, and the resulting film morphology. Large preaggregated structures present in the 1 min-stirred solution appear to survive, or at least influence, film morphology formation and serve as effective nucleation centers that promote molecular ordering during the rapid solvent evaporation of spin-casting. Consequently, the resulting film exhibits enhanced lamellar organization. In contrast, the 10 min-stirred solution, which contains the smallest aggregates due to optimal powder disintegration and minimal reaggregation, produces films with the weakest structural order. The 60 min-stirred solution, in which secondary aggregation has already begun, recovers some ordering ability but not to the extent of the 1 min case.

As shown in Figure 3c, the device efficiency exhibits a distinct dependence on the stirring duration of the polymer solution: 10 min (9.1%) > 60 min (5.7%) > 1 min (3.8%). The details will be discussed in the subsequent section. This trend suggests that there is an optimal stirring duration for achieving high performance. Insufficient stirring (e.g., 1 min) likely results in incomplete solvation and poor dispersion of the polymer, whereas excessive stirring (e.g., 60 min) promotes secondary aggregation, both of which lead to inferior film quality. To further investigate this relationship, atomic force microscopy (AFM) and Kelvin probe force microscopy (KPFM) were employed to assess the surface morphology and potential distribution of the polymer films prepared under different stirring conditions. As shown in Figure 3d and Figure S15, AFM analysis reveals that both the polymer film and the corresponding perovskite film deposited on the 10 min-stirred HTL display notably smoother and more uniform surfaces than those prepared under the other conditions, thereby promoting more intimate interfacial contact between adjacent layers. Similarly, the KPFM potential maps (Figure S16) reveal a minimum contact potential difference (CPD) RMS variation of 2.59 mV for the 10 min sample, compared with 2.74 mV and 2.64 mV for 1 min and 60 min samples, respectively, further confirming that this stirring time produces more homogeneous and high-quality HTL films. Overall, these findings suggest that mesoscale aggregates in solution play a key role during film formation, with larger aggregates functioning as structural seeds that facilitate polymer chain alignment and domain growth. Fine-tuning the solution stirring time therefore offers a straightforward strategy to control the degree of aggregation of the BDP-based polymers in solution and, consequently, the molecular ordering and nanostructure of the HTL films. Based on the results, all polymeric HTLs were fabricated using an optimal stirring duration of 10 min throughout this study.

Figure 4a illustrates the energy level alignment of TPSCs incorporating different polymeric HTLs, as determined by ultraviolet photoelectron spectroscopy (UPS). The corresponding raw UPS spectra are provided in Figure S17 of the Supporting Information. For efficient hole extraction, the valence band maximum (VBM) of the HTL is estimated to be − 5.08 eV for **PBDP-Ph**, − 5.05 eV for **PBTP**, and − 5.00 eV for **PBDP**, which ideally lie between those of the ITO substrate and the tin perovskite absorber. The removal of the electron-withdrawing Tz unit raises the highest occupied molecular orbital (HOMO) of **PBDP** relative to **PBTP**, whereas aryl substitution in **PBDP-Ph** lowers the HOMO energy level due to the weaker electron-donating nature of the 4-hexylphenyl side-chain relative to the traditional alkyl groups. A VBM closer to that of the perovskite facilitates more rapid hole transfer into the HTL, thereby reducing recombination losses and improving overall charge extraction. Notably, **PBDP-Ph** exhibits a VBM (−5.08 eV) closest to the perovskite (−5.12 eV), which directly correlates with its enhanced device performance.

To assess the quality of tin perovskite films deposited on different polymer HTLs, X-ray diffraction (XRD) measurements were performed to evaluate their crystallinity. As shown in Figure 4b, the perovskite film fabricated on **PBDP-Ph** exhibits the highest intensity at the main (100) diffraction peak at 14°, indicating superior crystallinity. Grazing-incidence wide-angle X-ray scattering (GIWAXS) was subsequently employed to examine the crystal orientation of the perovskite films. As shown in Figures 4c-e, the **PBDP-Ph**-based perovskite displays a more concentrated (100) diffraction signal along the q_z axis than those prepared on **PBTP** and **PBDP**, suggesting that the **PBDP-Ph** HTL suppresses random grain orientation and induces a preferential vertical alignment. Such orientation is expected to facilitate charge extraction across the film, thereby contributing to the superior device performance. The XRD and GIWAXS results reveal that perovskite films grown on **PBDP-Ph** HTL possess both the highest crystallinity and the most favorable orientation among the samples tested.

Given the high susceptibility of Sn^{2+} in Sn-based perovskite frameworks to oxidation, effectively mitigating this process is essential for achieving stable device operation. In this investigation, the conventional PEDOT:PSS HTL was replaced with three polymeric alternatives: **PBTP**, **PBDP**, and **PBDP-Ph**. The tin valence states were characterized via X-ray photoelectron spectroscopy (XPS) to assess the extent of oxidation suppression. As presented in Figures 4f-h, the relative Sn^{2+} contents for perovskites deposited on **PBDP-Ph**, **PBTP**, and **PBDP** were determined to be 97.57%, 95.00%, and 94.06%, respectively. Among these, the device incorporating **PBDP-Ph** exhibits the highest Sn^{2+} fraction, indicating its superior capacity to preserve the reduced state of tin and limits oxidative degradation. This oxidation suppression is attributed to the higher crystallinity and improved film compactness (as evidenced by the scanning electron microscopy (SEM) images discussed in the following section) of the **PBDP-Ph**-based perovskite, which likely hinder air permeation and thereby limit the oxidation of Sn^{2+} ions. In comparison, PEDOT:PSS-based devices show a significantly lower Sn^{2+} fraction (71.00%, Figure S18), highlighting the advantage of polymeric HTLs in mitigating tin oxidation.

To evaluate the roughness of the polymer HTLs, AFM measurements were conducted. As shown in Figure S19, the

https://doi.org/10.1021/acsenergylett.6c00952
ACS Energy Lett. XXXX, XXX, XXX−XXX

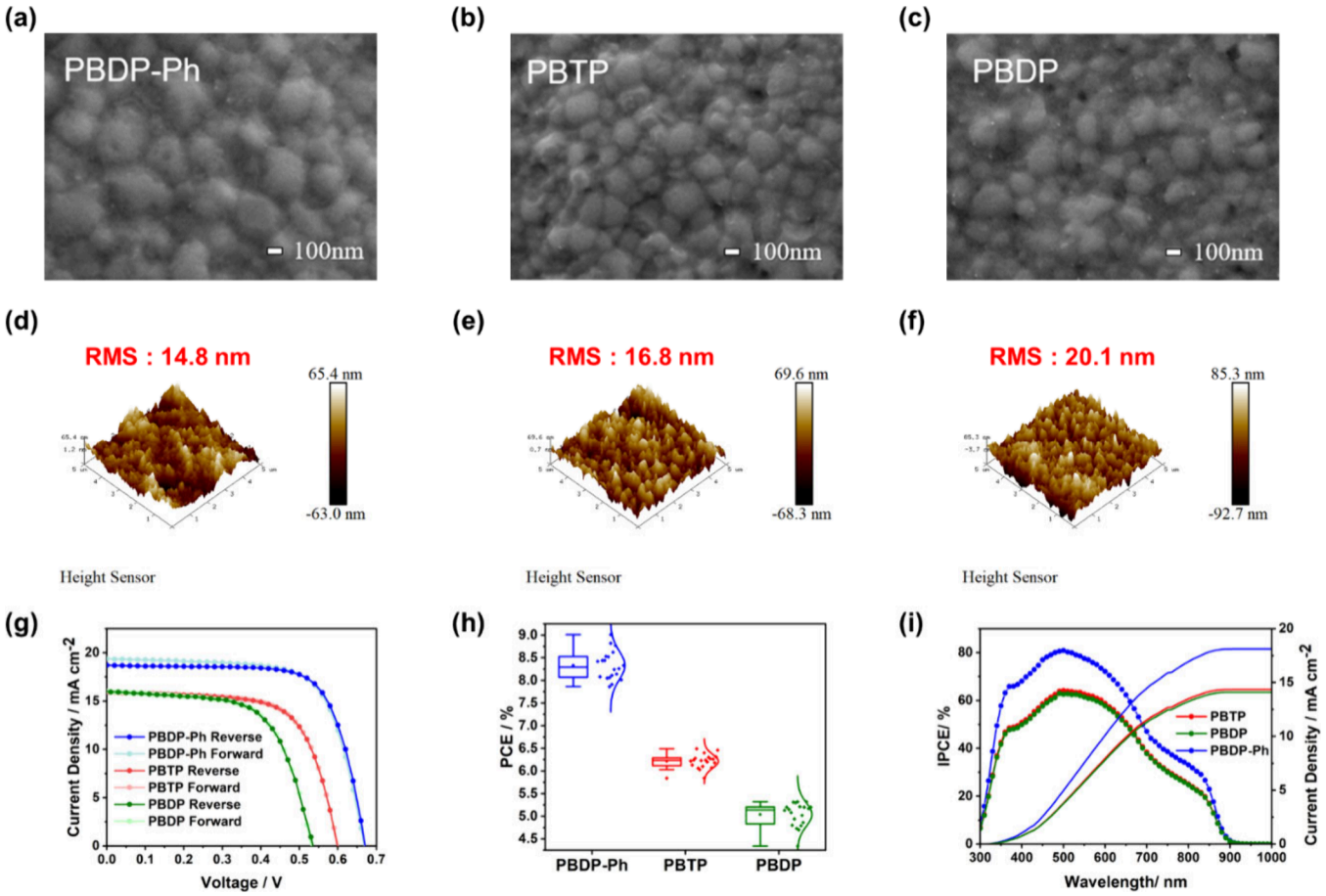

Figure 5. (a–c) Top-view SEM images of Sn-based perovskite films deposited on **PBDP-Ph**, **PBTP**, and **PBDP** HTLs. (d–f) Three-dimensional AFM images of Sn-based perovskite films fabricated on **PBDP-Ph**, **PBTP**, and **PBDP** HTLs. (g) *J-V* curves of TPSCs employing different polymer HTLs. (h) Statistical distribution of PCEs of 20 devices based on different HTLs. (i) IPCE spectra and the corresponding integrated current densities of TPSCs incorporating various HTLs.

PBDP-Ph film exhibits the lowest RMS roughness of 4.28 nm, compared to **PBTP** (4.55 nm) and **PBDP** (5.19 nm), which is favorable for subsequent Sn-based perovskite growth in inverted TPSCs. The smoother surface of **PBDP-Ph** film is attributed to aryl substituents that introduce steric hindrance, thereby suppressing excessive solution-state aggregation. The surface morphology of Sn-based perovskites films deposited on different polymeric HTLs were further examined by SEM and AFM. As shown in Figures 5a-c, top-view SEM images reveal that the perovskite film grown on **PBDP-Ph** exhibits larger grain sizes and fewer pinholes than those deposited on **PBTP** and **PBDP**, indicating a more uniform and compact film morphology. This improvement can be attributed to the smoother underlying HTL. The large grain size and reduced grain boundary density facilitate charge transport and thereby enhance the FF, while the decrease in pinholes reduces recombination loss and suppresses the oxidation of Sn^{2+}. Cross-sectional SEM images (Figure S20) further show that the **PBDP-Ph**-based perovskite film possesses the greatest thickness among the three (275, 240, and 215 nm for **PBDP-Ph**-, **PBTP**-, and **PBDP**-based perovskite films, respectively), suggesting that **PBDP-Ph** provides a more favorable environment for perovskite growth and thus improves light-harvesting ability of the device.

For efficient integration with the electron transport layer (ETL), the perovskite film should have low surface roughness to facilitate uniform ETL deposition. AFM measurements of the perovskite films (Figures 5d-f) show a clear RMS roughness trend with **PBDP-Ph** (14.8 nm) < **PBTP** (16.8 nm) < **PBDP** (20.1 nm), confirming that the **PBDP-Ph**-based perovskite film is the smoothest, which benefits interfacial contact with the ETL. Surface defect states in perovskite, such as uncoordinated Sn^{2+} or Sn^{4+} oxidized species, act as charge trapping centers that induce local electric fields and cause spatial fluctuations in the local work function, which are directly detected as variations in the CPD by KPFM. As shown in Figure S21, the **PBDP-Ph**-based film exhibits the smallest CPD RMS variation (2.59 mV), compared to 2.61 mV for **PBTP** and 2.71 mV for **PBDP**, indicating a more electronically homogeneous surface. This homogeneity implies a significant reduction in localized charge trapping, which correlates strongly with a lower density of surface defect states.

Three polymers were employed as HTLs to fabricate TPSCs with a p-i-n architecture: indium tin oxide (ITO)/polymer HTL/two-step Sn-based perovskite/C_{60}/bathocuproine (BCP)/Ag. The Sn-based perovskite layer was prepared via a two-step cosolvent-assisted method, which enables highly controlled nucleation and formation of a stable Sn^{2+}-rich intermediate phase. This process effectively suppresses rapid Sn^{2+} oxidation and enhances device operational stability compared to conventional one-step rapid-crystallization approaches. The current density–voltage (*J–V*) character-

https://doi.org/10.1021/acsenergylett.6c00952
ACS Energy Lett. XXXX, XXX, XXX–XXX

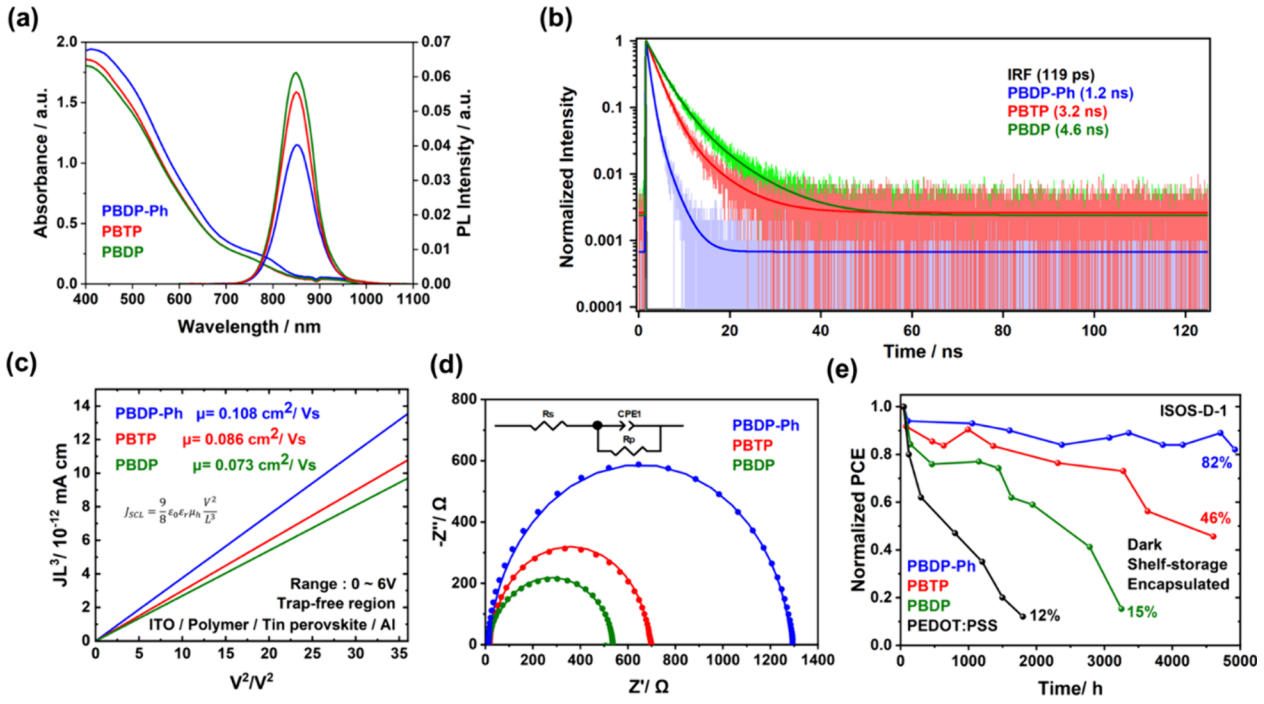

Figure 6. (a) PL and UV−vis absorption spectra of Sn-based perovskite films deposited on different polymer HTLs. (b) Time-resolved PL decay profiles obtained by TCSPC with multiexponential fitting. (c) SCLC characteristics of the polymer HTLs with fitting in the trap-free region. (d) EIS Nyquist plots and the corresponding equivalent-circuit fitting results for devices incorporating Sn-based perovskites deposited on the indicated polymer HTLs. (e) Long-term storage stability of the devices evaluated under the ISOS-D-1 protocol.

istics, including hysteresis, are shown in Figure 5g, and the photovoltaic parameters of the optimized champion devices are summarized in Table S2. Devices incorporating **PBDP-Ph** as the HTL deliver the highest PCE of 9.1%, outperforming those based on **PBTP** (6.50%) and **PBDP** (5.30%). This enhancement arises from the synergistic improvement of J_{SC}, V_{OC}, and FF, which can be attributed to the optimized solution-state aggregation and the resulting favorable HTL film morphology. In contrast, a control device employing PEDOT:PSS as the HTL achieves a much lower PCE of 3.9% (Figure S22). Notably, the 9.1% efficiency of **PBDP-Ph**-based device represents the highest reported value to date for two-step TPSCs employing non-PEDOT:PSS HTLs (Figure S23 and Table S3). Device reproducibility was evaluated using statistics from 20 independently fabricated devices, as presented in Figure 5h and Figure S24. In addition, incident photon-to-electron conversion efficiency (IPCE) measurements were conducted to validate the photocurrents of the devices. The integrated current densities obtained from the IPCE spectra (Figure 5i) closely match those derived from the $J-V$ curves, confirming the reliability of the device performance.

Beyond the morphology and crystallinity of Sn-based perovskite layers, charge-carrier dynamics play a pivotal role in determining device performance and operational stability. Figure 6a presents the steady-state photoluminescence (PL) and UV−vis absorption spectra of Sn-based perovskite films deposited on different polymeric HTLs. All samples exhibit identical PL peak positions, suggesting that the intrinsic emission properties of the perovskite are unaffected by the underlying HTLs. However, higher-efficiency devices exhibit stronger PL quenching, reflecting more effective hole extraction from perovskite into the HTL and reduced radiative recombination within the perovskite layer. To investigate charge extraction differences among HTLs, time-correlated single-photon counting (TCSPC) measurements were performed to monitor PL decay dynamics. The decay profiles were fitted using a multiexponential decay model; the corresponding fitting parameters are summarized in Table S4. As shown in Figure 6b, the perovskite film deposited on **PBDP-Ph** exhibits the shortest PL lifetime of 1.2 ns among the three samples (3.2 and 4.6 ns for **PBTP** and **PBDP**-based devices, respectively), indicating the most efficient and rapid hole extraction into the HTL for **PBDP-Ph**. While efficient interfacial hole extraction is essential, effective hole transport within the HTL toward the anode is also important for achieving high device performance. Therefore, the hole mobilities of the polymeric HTLs were evaluated using the space-charge-limited current (SCLC) method. As presented in Figure 6c, **PBDP-Ph**-based HTL shows the highest hole mobility (μ) of 0.108 cm^2/V s, compared with 0.086 and 0.073 cm^2/V s for **PBTP**- and **PBDP**-based devices, respectively. This enhancement is attributed to the TAA-type structural motif, where aryl substitution on the pyrrole nitrogen stabilizes the radical cation, thereby facilitating efficient hole transport. This high hole mobility contributes to rapid charge transport through the HTL, thereby contributing to the superior device performance. Efficient charge transport further minimizes recombination losses. To assess this, electrochemical impedance spectroscopy (EIS) measurements were conducted. Nyquist plots fitted using an equivalent circuit model (Figure 6d) reveal that the charge recombination resistance in the devices follows the order **PBDP-Ph** > **PBTP** > **PBDP**. This result confirms that **PBDP-Ph** not only enables fast hole extraction and high hole mobility but also suppresses charge recombination during transport, collectively leading to its outstanding photovoltaic performance.

https://doi.org/10.1021/acsenergylett.6c00952
ACS Energy Lett. XXXX, XXX, XXX−XXX

In addition to performance, long-term stability is a key challenge for TPSCs. Figure 6e summarizes the long-term storage stability evaluated using the ISOS-D-1 protocol. Device based on **PBDP-Ph** retain approximately 80% of its initial PCE after 5000 h of storage, whereas devices employing **PBTP** and **PBDP** show more pronounced degradation, retaining less than 50% of their initial efficiencies after 4000 h. In stark contrast, the device using PEDOT:PSS exhibits severe performance decay, retaining less than 20% of its initial efficiency within 2000 h, which can be attributed to the intrinsic hydrophilicity of PEDOT:PSS. The extended lifespans observed for **PBDP-Ph**-based devices are attributed to the higher crystallinity and more compact morphology of the corresponding perovskite films, which inhibit Sn^{2+} oxidation and thereby enhance device stability. Operational stability was further assessed by maximum power point tracking (MPPT) measurements under continuous illumination following the ISOS-S-1 protocol. As shown in Figure S25, the **PBDP-Ph**-based device maintains about 90% of its peak power output during a 5 h light-soaking test, further confirming its excellent operational stability.

In conclusion, we have developed a series of benzodipyrrole (BDP)-based conjugated polymer hole-transport materials for inverted tin perovskite solar cells and systematically elucidated the combined roles of molecular design and solution-state aggregation on device performance. Incorporation of a rigid and coplanar BDP ladder backbone, along with triarylamine-like aryl substitution, affords the polymer **PBDP-Ph** with favorable energy-level alignment, high hole mobility, and improved interfacial compatibility with tin perovskites. In addition, we identify the stirring time of the polymer precursor solution as a simple yet decisive processing parameter that governs polymer aggregation, thin-film morphology, and perovskite crystallization. An optimized stirring duration of 10 min yields uniform **PBDP-Ph** film, suppressed nonradiative recombination, and enhanced charge extraction. As a result, the **PBDP-Ph** device achieved a PCE of 9.1% via a two-step fabrication, along with markedly improved long-term and operational stability with T_{80} stability at 5000 h, outperforming other devices and PEDOT:PSS-based counterpart. These results highlight BDP-based ladder polymers as a viable material platform for hole-transport layers to advance efficient and stable tin-based perovskite solar cells.

■ ASSOCIATED CONTENT

Supporting Information

The Supporting Information is available free of charge at https://pubs.acs.org/doi/10.1021/acsenergylett.6c00952.

Materials and Characterization, Chemicals of Perovskite, Device Fabrication, Characterizations of Films and Devices, Synthetic Procedures, ^{1}H and ^{13}C NMR spectra Supplementary Figures, and Supplementary Tables (PDF)

■ AUTHOR INFORMATION

Corresponding Authors

Eric Wei-Guang Diau − *Department of Applied Chemistry and Institute of Molecular Science, National Yang Ming Chiao Tung University, Hsinchu 300093, Taiwan; Center for Emergent Functional Matter Science, National Yang Ming Chiao Tung University, Hsinchu 30010, Taiwan;* orcid.org/0000-0001-6113-5679; Email: diau@nycu.edu.tw

Yen-Ju Cheng − *Department of Applied Chemistry, National Yang Ming Chiao Tung University, Hsinchu 30010, Taiwan; Department of Applied Chemistry and Institute of Molecular Science, National Yang Ming Chiao Tung University, Hsinchu 300093, Taiwan;* orcid.org/0000-0003-0780-4557; Email: yjcheng@nycu.edu.tw

Authors

Chia-Fang Lu − *Department of Applied Chemistry, National Yang Ming Chiao Tung University, Hsinchu 30010, Taiwan*

Yun-Sheng Shih − *Department of Applied Chemistry and Institute of Molecular Science, National Yang Ming Chiao Tung University, Hsinchu 300093, Taiwan*

Chun-Hsiao Kuan − *Department of Applied Chemistry and Institute of Molecular Science, National Yang Ming Chiao Tung University, Hsinchu 300093, Taiwan*

Yu-An Ko − *Department of Applied Chemistry and Institute of Molecular Science, National Yang Ming Chiao Tung University, Hsinchu 300093, Taiwan*

Hsin-Lung Chen − *Department of Chemical Engineering, National Tsing Hua University, Hsinchu 30013, Taiwan;* orcid.org/0000-0002-3572-723X

Complete contact information is available at: https://pubs.acs.org/10.1021/acsenergylett.6c00952

Author Contributions

⊥Chia-Fang Lu and Yun-Sheng Shih equally contributed to this work.

Notes

The authors declare no competing financial interest.

■ ACKNOWLEDGMENTS

The authors thank Dr. B.-H. Liu and Dr. C.-H. Wang (TLS 24A1, NSRRC) for assistance with UPS and XPS analysis, and Dr. Y.-W. Tsai and Dr. J.-M. Lin (TPS 25A1, NSRRC) for support with GIWAXS measurements. FEG-SEM experiments were carried out at the Instrumentation Center of National Taiwan University with the help of Ms. Y.-T. Lee and Prof. C.-S. Lin. This work was supported by the National Science and Technology Council (NSTC), Taiwan (grant nos. 112-2636-M-009-006, 113-2639-M-A49-001-ASP, 113-2113-M-A49−015 -MY3, and 114-2639-M-A49-001-ASP), and by the Center for Emergent Functional Matter Science, National Yang Ming Chiao Tung University (NYCU), through the Featured Areas Research Center Program within the Higher Education Sprout Project of the Ministry of Education (MOE), Taiwan.

■ REFERENCES

(1) Xiong, Z.; Zhang, Q.; Cai, K.; Zhou, H.; Song, Q.; Han, Z.; Kang, S.; Li, Y.; Jiang, Q.; Zhang, X.; You, J. Homogenized Chlorine Distribution for >27% Power Conversion Efficiency in Perovskite Solar Cells. *Science* **2025**, *390*, 638−642.

(2) National Renewable Energy Laboratory, Best Research-Cell Efficiency Chart. https://www.nlr.gov/pv/cell-efficiency (accessed February 5, 2026).

(3) He, D.; Chen, P.; Steele, J. A.; Wang, Z.; Xu, H.; Zhang, M.; Ding, S.; Zhang, C.; Lin, T.; Kremer, F.; Xu, H.; Hao, M.; Wang, L. Homogeneous 2D/3D Heterostructured Tin Halide Perovskite Photovoltaics. *Nat. Nanotechnol.* **2025**, *20*, 779−786.

(4) Li, T.; Luo, X.; Wang, P.; Li, Z.; Li, Y.; Huang, J.; Jin, Z.; Yang, Y.; Li, B.; Zhang, W.; Lin, S.; Rui, Y.; Wang, H.; Zhang, Q.; Zhan, Y.; Xu, B.; Liang, J.; Qi, Y. Tin-Based Perovskite Solar Cells with A Homogeneous Buried Interface. *Nature* **2025**, *648*, 84−90.
(5) Shahbazi, S.; Li, M.-Y.; Fathi, A.; Diau, E. W.-G. Realizing a Cosolvent System for Stable Tin-Based Perovskite Solar Cells Using a Two-Step Deposition Approach. *ACS Energy Lett.* **2020**, *5*, 2508−2511.
(6) Rajamanickam, P.; Tiwari, I.; Nebhani, L.; Diau, E. W.-G. Multifunctional Engineering-Enabled Electron Transport in SnO2 for Sn-Based Perovskite Solar Cells in the nip Configuration. *ACS Appl. Mater. Interfaces* **2025**, *17*, 49584−49593.
(7) Song, D.; Narra, S.; Li, M.-Y.; Lin, J.-S.; Diau, E. W.-G. Interfacial Engineering with a Hole-Selective Self-Assembled Monolayer for Tin Perovskite Solar Cells via a Two-Step Fabrication. *ACS Energy Lett.* **2021**, *6*, 4179−4186.
(8) Abid, A.; Rajamanickam, P.; Diau, E. W.-G. Design of a Simple Bifunctional System As a Self-Assembled Monolayer (SAM) for Inverted Tin-Based Perovskite Solar Cells. *J. Chem. Eng.* **2023**, *477*, 146755.
(9) Kuan, C.-H.; Luo, G.-S.; Narra, S.; Maity, S.; Hiramatsu, H.; Tsai, Y.-W.; Lin, J.-M.; Hou, C.-H.; Shyue, J.-J.; Diau, E. W.-G. How can a hydrophobic polymer PTAA serve as a hole-transport layer for an inverted tin perovskite solar cell? *J. Chem. Eng.* **2022**, *450*, 138037.
(10) Choi, H.; Mai, C.-K.; Kim, H.-B.; Jeong, J.; Song, S.; Bazan, G. C.; Kim, J. Y.; Heeger, A. J. Conjugated Polyelectrolyte Hole Transport Layer for Inverted-type Perovskite Solar Cells. *Nat. Commun.* **2015**, *6*, 7348.
(11) Zhan, L.; Zhang, L.; Li, Y.; Cai, H.; Wu, Y. Performance and Stability Enhancement of Hole-Transporting Materials in Inverted Perovskite Solar Cells. *ACS Appl. Energy Mater.* **2025**, *8*, 3985−3996.
(12) Heo, J. H.; Han, H. J.; Kim, D.; Ahn, T. K.; Im, S. H. Hysteresis-Less Inverted CH 3 NH 3 PbI 3 Planar Perovskite Hybrid Solar Cells with 18.1% Power Conversion Efficiency. *Energy Environ. Sci.* **2015**, *8*, 1602−1608.
(13) Guo, H.; Wang, X.; Li, C.; Hu, H.; Zhang, H.; Zhang, L.; Zhu, W. H.; Wu, Y. Immobilizing Surface Halide in Perovskite Solar Cells via Calix[4]pyrrole. *Adv. Mater.* **2023**, *35*, 2301871.
(14) Azmi, R.; Ugur, E.; Seitkhan, A.; Aljamaan, F.; Subbiah, A. S.; Liu, J.; Harrison, G. T.; Nugraha, M. I.; Eswaran, M. K.; Babics, M.; Chen, Y.; Xu, F.; Allen, T. G.; Rehman, A. u.; Wang, C.-L.; Anthopoulos, T. D.; Schwingenschlögl, U.; De Bastiani, M.; Aydin, E.; De Wolf, S. Damp Heat-Stable Perovskite Solar Cells with Tailored-Dimensionality 2D/3D Heterojunctions. *Science* **2022**, *376*, 73−77.
(15) Chin, X. Y.; Turkay, D.; Steele, J. A.; Tabean, S.; Eswara, S.; Mensi, M.; Fiala, P.; Wolff, C. M.; Paracchino, A.; Artuk, K.; Jacobs, D.; Guesnay, Q.; Sahli, F.; Andreatta, G.; Boccard, M.; Jeangros, Q.; Ballif, C. Interface Passivation for 31.25%-Efficient Perovskite/Silicon Tandem Solar Cells. *Science* **2023**, *381*, 59−63.
(16) Li, L.; Wang, Y.; Wang, X.; Lin, R.; Luo, X.; Liu, Z.; Zhou, K.; Xiong, S.; Bao, Q.; Chen, G.; Tian, Y.; Deng, Y.; Xiao, K.; Wu, J.; Saidaminov, M. I.; Lin, H.; Ma, C.-Q.; Zhao, Z.; Wu, Y.; Zhang, L.; Tan, H. Flexible All-Perovskite Tandem Solar Cells Approaching 25% Efficiency with Molecule-Bridged Hole-Selective Contact. *Nat. Energy* **2022**, *7*, 708−717.
(17) He, R.; Wang, W.; Yi, Z.; Lang, F.; Chen, C.; Luo, J.; Zhu, J.; Thiesbrummel, J.; Shah, S.; Wei, K.; Luo, Y.; Wang, C.; Lai, H.; Huang, H.; Zhou, J.; Zou, B.; Yin, X.; Ren, S.; Hao, X.; Wu, L.; Zhang, J.; Zhang, J.; Stolterfoht, M.; Fu, F.; Tang, W.; Zhao, D. Improving Interface Quality for 1-cm2 All-Perovskite Tandem Solar Cells. *Nature* **2023**, *618*, 80−86.
(18) Min, H.; Kim, M.; Lee, S.-U.; Kim, H.; Kim, G.; Choi, K.; Lee, J. H.; Seok, S. I. Efficient, Stable Solar Cells by Using Inherent Bandgap of α-Phase Formamidinium Lead iIodide. *Science* **2019**, *366*, 749−753.
(19) Yi, C.; Luo, J.; Meloni, S.; Boziki, A.; Ashari-Astani, N.; Grätzel, C.; Zakeeruddin, S. M.; Röthlisberger, U.; Grätzel, M. Entropic Stabilization of Mixed A-Cation ABX 3 Metal Halide Perovskites for High Performance Perovskite Solar Cells. *Energy Environ. Sci.* **2016**, *9*, 656−662.
(20) Zheng, X.; Chen, B.; Dai, J.; Fang, Y.; Bai, Y.; Lin, Y.; Wei, H.; Zeng, X. C.; Huang, J. Defect Passivation in Hybrid Perovskite Solar Cells Using Quaternary Ammonium Halide Anions and Cations. *Nat. Energy* **2017**, *2*, 1−9.
(21) Zhao, Y.; Zhu, K. Organic-Inorganic Hybrid Lead Halide Perovskites for Optoelectronic and Electronic Applications. *Chem. Soc. Rev.* **2016**, *45*, 655−689.
(22) Truong, M. A.; Funasaki, T.; Ueberricke, L.; Nojo, W.; Murdey, R.; Yamada, T.; Hu, S.; Akatsuka, A.; Sekiguchi, N.; Hira, S.; Xie, L.; Nakamura, T.; Shioya, N.; Kan, D.; Tsuji, Y.; Iikubo, S.; Yoshida, H.; Shimakawa, Y.; Hasegawa, T.; Kanemitsu, Y.; Suzuki, T.; Wakamiya, A. Tripodal Triazatruxene Derivative as a Face-On Oriented HoleCollecting Monolayer for Efficient and Stable Inverted Perovskite Solar Cells. *J. Am. Chem. Soc.* **2023**, *145*, 7528−7539.
(23) Magomedov, A.; Al-Ashouri, A.; Kasparavičius, E.; Strazdaite, S.; Niaura, G.; Jošt, M.; Malinauskas, T.; Albrecht, S.; Getautis, V. Self-Assembled Hole Transporting Monolayer for Highly Efficient Perovskite Solar Cells. *Adv. Energy Mater.* **2018**, *8*, 1801892.
(24) Xu, X.; Ji, X.; Chen, R.; Ye, F.; Liu, S.; Zhang, S.; Chen, W.; Wu, Y.; Zhu, W. H. Improving Contact and Passivation of Buried Interface for High-Efficiency and Large-Area Inverted Perovskite Solar Cells. *Adv. Funct. Mater.* **2022**, *32*, 2109968.
(25) Sun, X.; Li, Z.; Yu, X.; Wu, X.; Zhong, C.; Liu, D.; Lei, D.; Jen, A. K. Y.; Li, Z. a.; Zhu, Z. Efficient Inverted Perovskite Solar Cells with Low Voltage Loss Achievedbya Pyridine-Based Dopant-Free Polymer Semiconductor. *Angew. Chem., Int. Ed.* **2021**, *60*, 7227−7233.
(26) Liu, Z.; Li, S.; Wang, X.; Cui, Y.; Qin, Y.; Leng, S.; Xu, Y.-x.; Yao, K.; Huang, H. Interfacial Engineering of Front-Contact with Finely Tuned Polymer Interlayers for High-Performance Large-Area Flexible Perovskite Solar Cells. *Nano Energy* **2019**, *62*, 734−744.
(27) Hung, C. M.; Chih, C. J.; Huang, K. H.; Xue, Y. J.; Chu, H. C.; Tseng, C. C.; Li, C. H.; Chen, J. Y.; Chen, B. H.; Yang, S. D.; Cheng, Y.-J.; Chou, P.-T. Perovskite-Coupled NIR Organic Hybrid Solar Cells Achieving an 84.2% Fill Factor and a 25.2% Efficiency: A Comprehensive Mechanistic Exploration. *Angew. Chem., Int. Ed.* **2025**, *64*, No. e202501375.
(28) Fang, R.; Wu, S.; Chen, W.; Liu, Z.; Zhang, S.; Chen, R.; Yue, Y.; Deng, L.; Cheng, Y.-B.; Han, L.; Chen, W. [6,6]-Phenyl-C61-Butyric Acid Methyl Ester/ Cerium Oxide Bilayer Structure as Efficient and Stable Electron Transport Layer for Inverted Perovskite Solar Cells. *ACS Nano* **2018**, *12*, 2403−2414.
(29) Li, Z.; Li, B.; Wu, X.; Sheppard, S. A.; Zhang, S.; Gao, D.; Long, N. J.; Zhu, Z. Organometallic-Functionalized Interfaces for Highly Efficient Inverted Perovskite Solar Cells. *Science* **2022**, *376*, 416−420.
(30) Li, T.; He, F.; Liang, J.; Qi, Y. Functional Layers in Efficient and Stable Inverted Tin-based Perovskite Solar Cells. *Joule* **2023**, *7*, 1966−1991.
(31) Li, T.; Zhang, Z.; He, F.; Deng, L.; Yang, Y.; Mo, X.; Zhan, Y.; Liang, J. Alleviating the Crystallization Dynamics and Suppressing the Oxidation Process for Tin-Based Perovskite Solar Cells with Fill Factors Exceeding 80%. *Adv. Funct. Mater.* **2023**, *33*, 2308457.
(32) Li, T.; Li, B.; Yang, Y.; Jin, Z.; Zhang, Z.; Wang, P.; Deng, L.; Zhan, Y.; Zhang, Q.; Liang, J. Metal Chalcogenide Electron Extraction Layers for nip-Type Tin-based Perovskite Solar Cells. *Nat. Commun.* **2024**, *15*, 9435.
(33) Balasaravanan, R.; Kuan, C.-H.; Shih, Y.-S.; Cheng, H.-L.; Ganesan, D.; Hong, S.-H.; Liu, C.-L.; Zhong, Y.-R.; Jiang, X.; Chen, M.-C.; Diau, E. W. G. Electron "Push-Push-Pull" Type Dithienopyrrole-Based Self-Assembled Monolayers on NiOx for Enhanced Performance of Tin Perovskite Solar Cells. *J. Chem. Eng.* **2025**, *519*, 165231.
(34) Kuan, C. H.; Balasaravanan, R.; Hsu, S. M.; Ni, J. S.; Tsai, Y. T.; Zhang, Z. X.; Chen, M. C.; Diau, E. W. G. Dopant-Free Pyrrolopyrrole-Based (PPr) PolymericHole-Transporting Materials for Efficient Tin-Based Perovskite Solar Cells with Stability Over 6000 h. *Adv. Mater.* **2023**, *35*, 2300681.

https://doi.org/10.1021/acsenergylett.6c00952
ACS Energy Lett. XXXX, XXX, XXX−XXX

(35) Song, D.; Shin, S. W.; Wu, H.-P.; Diau, E. W.-G.; Correa-Baena, J.-P. Toward Maximizing Hole Selection with Self-Assembled Monolayers in Sn-Based Perovskite Solar Cells. *ACS Energy Lett.* **2025**, *10*, 1292−1312.
(36) Zhou, H.; Sheng, W.; Rao, H.; Su, Y.; Zhu, W.; Zhong, Y.; Liu, Y.; He, J.; Tan, L.; Chen, Y. Reaction-Diffusion and Crystallization Kinetics Modulation of Two-Step Deposited Tin-Based Perovskite Film via Reducing Atmosphere. *Angew. Chem., Int. Ed.* **2025**, *137*, No. e202422217.
(37) Balasaravanan, R.; Kuan, C. H.; Hsu, S. M.; Chang, E. C.; Chen, Y. C.; Tsai, Y. T.; Jhou, M. L.; Yau, S. L.; Liu, C. L.; Chen, M. C.; Diau, E. W. G. Triphenylamine (TPA)-Functionalized Structural Isomeric Polythiophenes as Dopant Free Hole-Transporting Materials for Tin Perovskite Solar Cells. *Adv. Energy Mater.* **2023**, *13*, 2302047.
(38) Cheng, Y.-J.; Yang, S.-H.; Hsu, C.-S. Synthesis of Conjugated Polymers for Organic Solar Cell Applications. *Chem. Rev.* **2009**, *109*, 5868−5923.
(39) Wu, J.-S.; Cheng, S.-W.; Cheng, Y.-J.; Hsu, C.-S. Donor-Acceptor Conjugated Polymers Based on Multifused Ladder-Type Arenes for Organic Solar Cells. *Chem. Soc. Rev.* **2015**, *44*, 1113−1154.
(40) Cheng, Y.-J.; Ho, Y.-J.; Chen, C.-H.; Kao, W.-S.; Wu, C.-E.; Hsu, S.-L.; Hsu, C.-S. Synthesis, Photophysical and Photovoltaic Properties of Conjugated Polymers Containing Fused Donor-Acceptor Dithienopyrrolobenzothiadiazole and Dithienopyrroloquinoxaline Arenes. *Macromolecules* **2012**, *45*, 2690−2698.
(41) Cheng, Y.-J.; Chen, C.-H.; Ho, Y.-J.; Chang, S.-W.; Witek, H. A.; Hsu, C.-S. Thieno[3,2-b]pyrrolo Donor Fused with Benzothiadiazolo, Benzoselenadiazolo and Quinoxalino Acceptors: Synthesis, Characterization, and Molecular Properties. *Org. Lett.* **2011**, *13*, 5484−5487.
(42) Cui, Y.; Yao, H.; Zhang, J.; Xian, K.; Zhang, T.; Hong, L.; Wang, Y.; Xu, Y.; Ma, K.; An, C.; He, C.; Wei, Z.; Gao, F.; Hou, J. Single-Junction Organic Photovoltaic Cells with Approaching 18% Efficiency. *Adv. Mater.* **2020**, *32*, 1908205.
(43) Li, C.; Zhou, J.; Song, J.; Xu, J.; Zhang, H.; Zhang, X.; Guo, J.; Zhu, L.; Wei, D.; Han, G.; Min, J.; Zhang, Y.; Xie, Z.; Yi, Y.; Yan, H.; Gao, F.; Liu, F.; Sun, Y. Non-fullerene Acceptors with Branched Side Chains and Improved Molecular Packing to Exceed 18% Efficiency in Organic Solar Cells. *Nat. Energy* **2021**, *6*, 605−613.
(44) Yuan, J.; Zhang, Y.; Zhou, L.; Zhang, G.; Yip, H.-L.; Lau, T.-K.; Lu, X.; Zhu, C.; Peng, H.; Johnson, P. A.; Leclerc, M.; Cao, Y.; Ulanski, J.; Li, Y.; Zou, Y. Single-Junction Organic Solar Cell with Over 15% Efficiency Using Fused-Ring Acceptor with Electron-Deficient Core. *Joule* **2019**, *3*, 1140−1151.
(45) Tian, L.; Liu, C.; Huang, F. Recent Progress in Side Chain Engineering of Y-Series Non-Fullerene Molecule and Polymer Acceptors. *Science China Chemistry* **2024**, *67*, 788−805.
(46) Hai, J.; Wu, H.; Yin, X.; Song, J.; Hu, L.; Jin, Y.; Li, L.; Su, Z.; Xu, Z.; Wang, H.; Li, Z. Dopant-Free Hole Transport Materials Based on a Large Conjugated Electron-Deficient Core for Efficient Perovskite Solar Cells. *Adv. Funct. Mater.* **2021**, *31*, 2105458.
(47) Li, B.; Yang, J.; Liao, Q.; Ji, X.; Wang, Y.; Yang, J.; Liu, B.; Liang, Q.; Wang, Z.; Li, H.; Wang, K.; Sun, H.; Niu, L.; Guo, X. Dopant-Free Polymeric Hole Transport Materials with a DA'D-A Backbone for Efficient and Stable Inverted Perovskite Solar Cells. *Solar RRL.* **2024**, *8*, 2300740.
(48) Wang, Y.-D.; Wang, Y.; Shao, J.-Y.; Lan, Y.; Lan, Z.-R.; Zhong, Y.-W.; Song, Y. Defect Passivation by a D-A-D Type Hole-Transporting Interfacial Layer for Efficient and Stable Perovskite Solar Cells. *ACS Energy Lett.* **2021**, *6*, 2030−2037.
(49) Zhao, X.; Quan, Y.; Pan, H.; Li, Q.; Shen, Y.; Huang, Z.-S.; Wang, M. Novel Donor-Acceptor-Donor Structured Small Molecular Hole Transporting Materials for Planar Perovskite Solar Cells. *Adv. Electron. Mater.* **2019**, *32*, 85−92.
(50) Shi, Z.-E.; Fu, Y.-F.; Peng, B.-S.; Hung, T.-C.; Ganesan, D.; Balasaravanan, R.; Hong, S.-H.; Liu, C.-L.; Su, C.-J.; Chen, M.-C.; Chen, C.-P. Tailoring Anchoring Functionalities of Self-Assembled Materials for Efficient Wide-Bandgap Perovskite Solar Cells. *J. Chem. Eng.* **2025**, *526*, 171321.
(51) Xue, Y.-J.; Lai, Z.-Y.; Lu, H.-C.; Hong, J.-C.; Tsai, C.-L.; Huang, C.-L.; Huang, K.-H.; Lu, C.-F.; Lai, Y.-Y.; Hsu, C.-S.; Lin, J.-M.; Chang, J.-W.; Chien, S.-Y.; Lee, G.-H.; Jeng, U.-S.; Cheng, Y.-J. Unraveling the Structure-Property-Performance Relationships of Fused-Ring Nonfullerene Acceptors: Toward a C-Shaped ortho-Benzodipyrrole-Based Acceptor for Highly Efficient Organic Photovoltaics. *J. Am. Chem. Soc.* **2024**, *146*, 833−848.
(52) Huang, K.-H.; Tseng, C.-C.; Tsai, C.-L.; Xue, Y.-J.; Lu, H.-C.; Lu, C.-F.; Chang, Y.-Y.; Huang, C.-L.; Hsu, I.-J.; Lai, Y.-Y.; Zheng, Y.-P.; Jiang, B.-H.; Chen, C.-P.; Chien, S.-Y.; Jeng, U.-S.; Hsu, C.-S.; Cheng, Y.-J. Highly Crystalline Selenium-Substituted C-Shaped Ortho-Benzodipyrrole-Based A-D-A-Type Nonfullerene Acceptor Enabling Solution-Processed Single-Crystal-Like Thin Films for Air-Stable, High-Mobility N-Type Transistors. *Adv. Funct. Mater.* **2025**, *35*, 2419176.
(53) Lu, C.-F.; Huang, Y.-C.; Lin, L.-Y.; Xue, Y.-J.; Huang, K.-H.; Tsai, C.-L.; Wu, C.-S.; Chien, S.-Y.; Lin, K.-H.; Cheng, Y.-J. Side-Chain-Modulated Charge Transport Polarity in Curved Ortho-Benzodipyrrole-Based Acceptors for High-Performance Organic Photovoltaics and Transistors. *Chem. Mater.* **2025**, *37*, 8901−8915.
(54) Hung, C.-M.; Chih, C.-J.; Huang, K.-H.; Xue, Y.-J.; Chu, H.-C.; Tseng, C.-C.; Li, C.-H.; Chen, J.-Y.; Chen, B.-H.; Yang, S.-D.; Cheng, Y.-J.; Chou, P.-T. Perovskite-Coupled NIR Organic Hybrid Solar Cells Achieving an 84.2% Fill Factor and a 25.2% Efficiency: A Comprehensive Mechanistic Exploration. *Angew. Chem., Int. Ed.* **2025**, *64*, No. e202501375.
(55) Wang, Y.-B.; Tsai, C.-L.; Xue, Y.-J.; Jiang, B.-H.; Lu, H.-C.; Hong, J.-C.; Huang, Y.-C.; Huang, K.-H.; Chien, S.-Y.; Chen, C.-P.; Cheng, Y.-J. Fluorinated and Methylated Ortho-Benzodipyrrole-Based Acceptors Suppressing Charge Recombination and Minimizing Energy Loss in Organic Photovoltaics. *Chem. Sci.* **2025**, *16*, 3259−3274.
(56) Xue, Y.-J.; Chang, C.-Y.; Hung, C.-M.; Tseng, C.-C.; Chang, J.-W.; Su, C.-J.; Tsai, C.-L.; Lu, H.-C.; Huang, K.-H.; Tai, K.-Y.; Ku, C.-Y.; Wu, C.-S.; Chien, S.-Y.; Yang, S.-D.; Jiang, B.-H.; Chen, C.-P.; Chou, P.-T.; Jeng, U.-S.; Cheng, Y.-J. Side-Chains Engineered Self-Assembly of Ortho-Benzodipyrrole-Based Acceptors: Comprehensive Exploration of Structure-Interface-Photovoltaics Correlations. *Adv. Funct. Mater.* **2025**, *35*, No. e04705.
(57) Wang, Y.-B.; Xue, Y.-J.; Hung, C.-M.; Huang, K.-H.; Jiang, B.-H.; Tsai, C.-L.; Huang, Y.-C.; Chen, H.-Y.; Yang, S.-D.; Chien, S.-Y.; Chen, C.-P.; Chou, P.-T.; Cheng, Y.-J. Effect of Halogen/Chalcogen Substitution on The Dielectric Constant of Asymmetric Acceptor Alloy to Improve The Efficiency And Stability of Inverted Organic Photovoltaics. *Chem. Sci.* **2025**, *16*, 17391−17407.
(58) Chang, Y.-Y.; Tsai, C.-L.; Xue, Y.-J.; Wang, Y.-B.; Huang, K.-H.; Huang, Y.-C.; Tseng, C.-C.; Lee, J.; Jiang, B.-H.; Chen, C.-P.; Cheng, Y.-J. Side-Chain Engineering of C-Shaped Ortho-Benzodipyrrole-Based A-D-A Acceptors for Energy Loss Suppression in Organic Photovoltaics. *J. Mater. Chem. A* **2025**, *13*, 36500−36512.
(59) Wang, Y.-B.; Xue, Y.-J.; Chen, H.-Y.; Tsai, C.-L.; Lee, J.; Jiang, B.-H.; Chen, C.-P.; Chen, F.-C.; Hsu, C.-S.; Chu, T.-Y.; Lu, J.; Chien, S.-Y.; Cheng, Y.-J. Fluorinated Benzodipyrrole-Based Non-Fullerene Acceptors with Chlorinated End Groups Exhibiting Fluorine-Chlorine Interactions for Suppressed Charge Recombination in Organic Photovoltaics. *ACS Appl. Mater. Interfaces* **2026**, *18*, 10138.
(60) Balasaravanan, R.; Kuan, C. H.; Hsu, S. M.; Chang, E. C.; Chen, Y. C.; Tsai, Y. T.; Jhou, M. L.; Yau, S. L.; Liu, C. L.; Chen, M. C.; Diau, E. W. G. Triphenylamine (TPA)-Functionalized Structural Isomeric Polythiophenes as Dopant Free Hole-Transporting Materialsfor Tin Perovskite Solar Cells. *Adv. Energy Mater.* **2023**, *13*, 2302047.
(61) Ke, W.; Priyanka, P.; Vegiraju, S.; Stoumpos, C. C.; Spanopoulos, I.; Soe, C. M. M.; Marks, T. J.; Chen, M.-C.; Kanatzidis, M. G. Dopant-Free Tetrakis-Triphenylamine Hole Transporting Material for Efficient Tin-Based Perovskite Solar Cells. *J. Am. Chem. Soc.* **2018**, *140*, 388−393.
(62) Vegiraju, S.; Ke, W.; Priyanka, P.; Ni, J. S.; Wu, Y. C.; Spanopoulos, I.; Yau, S. L.; Marks, T. J.; Chen, M. C.; Kanatzidis, M.

https://doi.org/10.1021/acsenergylett.6c00952
ACS Energy Lett. XXXX, XXX, XXX−XXX

G. Benzodithiophene Hole-Transporting Materials for Efficient Tin-Based Perovskite Solar Cells. *Adv. Funct. Mater.* **2019**, *29*, 1905393.
(63) Ji, X.; Feng, K.; Ma, S.; Wang, J.; Liao, Q.; Wang, Z.; Li, B.; Huang, J.; Sun, H.; Wang, K.; Guo, X. Interfacial Passivation Engineering for Highly Efficient Perovskite Solar Cells with a Fill Factor Over 83%. *ACS Nano* **2022**, *16*, 11902−11911.
(64) Cheng, Y.-J.; Liao, M.-H.; Shih, H.-M.; Shih, P.-I.; Hsu, C.-S. Exciplex Electroluminescence Induced by Cross-Linked Hole-Transporting Materials for White Light Polymer Light-Emitting Diodes. *Macromolecules* **2011**, *44*, 5968−5976.
(65) Schafer, E.; Sommer, M.; Ott, M. Time-Dependent Structure Assessment of Conjugated Polymer Aggregates in Solution by Single-Molecule Fluorescence Spectroscopy. *Macromolecules* **2026**, *59*, 1740−1751.
(66) Yao, Z.-F.; Wang, J.-Y.; Pei, J. Controlling Morphology and Microstructure of Conjugated Polymers via Solution-State Aggregation. *Prog. Polym. Sci.* **2023**, *136*, 101626.
(67) Park, Y. D.; Park, J. K.; Seo, J. H.; Yuen, J. D.; Lee, W. H.; Cho, K.; Bazan, G. C. Solubility-Controlled Structural Ordering of Narrow Bandgap Conjugated Polymers. *Adv. Energy Mater.* **2011**, *1*, 63−67.

https://doi.org/10.1021/acsenergylett.6c00952
ACS Energy Lett. XXXX, XXX, XXX−XXX